Scripta Materialia 186 (2020) 336–340

Contents lists available at ScienceDirect

Scripta Materialia

journal homepage: www.elsevier.com/locate/scriptamat

High-strength and high-ductility $AlCoCrFeNi_{2.1}$ eutectic high-entropy alloy achieved via precipitation strengthening in a heterogeneous structure

Ting Xiong[a,b], Shijian Zheng[a,c,*], Jingyu Pang[a,b], Xiuliang Ma[a,d]

[a] Shenyang National Laboratory for Materials Science, Institute of Metal Research, Chinese Academy of Sciences, 72 Wenhua Road, Shenyang 110016, China
[b] School of Material Science and Engineering, University of Science and Technology of China, Hefei 230026, China
[c] State Key Laboratory of Reliability and Intelligence of Electrical Equipment, Hebei University of Technology, Tianjin 300130, China
[d] School of Material Science and Engineering, Lanzhou University of Technology, 730050, Lanzhou, China

ARTICLE INFO

Article history:
Received 2 April 2020
Revised 24 April 2020
Accepted 24 April 2020

Keywords:
High-entropy alloys (HEAs)
Precipitation strengthening
Heterogeneous structure
High strength
High ductility

ABSTRACT

High-entropy alloys (HEAs) have displayed numerous unique features, however, high strength and high ductility are still the urgently desired mechanical property. The current study reports an outstanding combination of high strength and excellent ductility achieved in a eutectic high-entropy alloy (EHEA) $AlCoCrFeNi_{2.1}$. The great achievement relays on a dual-phase heterogeneous structure strengthened with nano-precipitates. The heterogeneous structure provides the alloy a good combination of strength and ductility, and nano-precipitates in both of the face-centered cubic (FCC) and B2 phases generate an extra significant contribution to strength.

Since proposed in 2004, the high-entropy alloys (HEAs) have received considerable interest for their unique properties, such as outstanding fracture resistance, superior irradiation resistance, and so on [1–3]. For manufacturing and load-bearing applications as structural materials, high strength accompanied with enough ductility is an important goal of the research of HEAs. At the early stage of HEAs research multiphase structure and intermetallic phase were deemed to be harmful to the mechanical property of the material, thereby being excluded in HEAs design [4,5]. As a result, the most studied HEAs systems exhibit single solid solution structure, such as face-centered-cubic (FCC) and body-centered-cubic (BCC) [2,6–8]. However, HEAs with single solid solution phase are often insufficient strong or too brittle to meet the engineering structural application [7,9].

Heterogeneous materials with widely distributed domains possessing dramatic difference in strength, such as gradient structure [10,11], heterogeneous lamella/layer structure [12,13], dual-phase steel [14], bimodal structure [15], etc., could achieve superior combinations of strength and ductility [16]. Recently, a number of studies reveled that multiphase HEAs consisting soft and hard phases showed significant enhancement in structural properties [17–19]. So the heterogeneous structure strengthening mechanism in traditional metallic material are proved to be suitable in the HEAs [20]. Among the multiphase HEAs, the EHEA $AlCoCrFeNi_{2.1}$ exhibiting alternating soft FCC and hard B2 lamellar is the most studied [21–23]. Moreover, the mechanical property of the EHEA can be further optimized by tailoring different heterogeneous structures through thermo-mechanical treatments [21–23].

Besides architecting heterogeneous microstructure [13,16,21–24], introducing coherent nanoprecipitate is also an effective method to strengthen the material meanwhile maintain enough ductility [25,26]. Previous composition analysis of the FCC/B2 dual-phase EHEA $AlCoCrFeNi_{2.1}$ showed that the FCC phase exhibited a composition of $Al_{6.43}Co_{21.14}Cr_{24.36}Fe_{24.16}Ni_{23.93}$, which is about equal to $Al_{0.3}CoCrFeNi$ [27]. Moreover, ordered $L1_2$ precipitates have been reported to be stable in an $Al_{0.3}CoCrFeNi$ FCC HEA between 550 °C to 700 °C [28]. Also, Wani et al. reported that a Cr-enriched phase is supposed to precipitate in the B2 phase under 800 °C [29]. According to the above researches, we can propose that different precipitates can be introduced into the FCC phase and the B2 phase, respectively.

In this work, nanoprecipitates are introduced into the EHEA with a heterogeneous structure through thermo-mechanical treat-

* Corresponding author at: Shenyang National Laboratory for Materials Science, Institute of Metal Research, Chinese Academy of Sciences, 72 Wenhua Road, Shenyang 110016, China.
E-mail addresses: sjzheng@imr.ac.cn, sjzheng@hebut.edu.cn (S. Zheng).

https://doi.org/10.1016/j.scriptamat.2020.04.035
1359-6462/

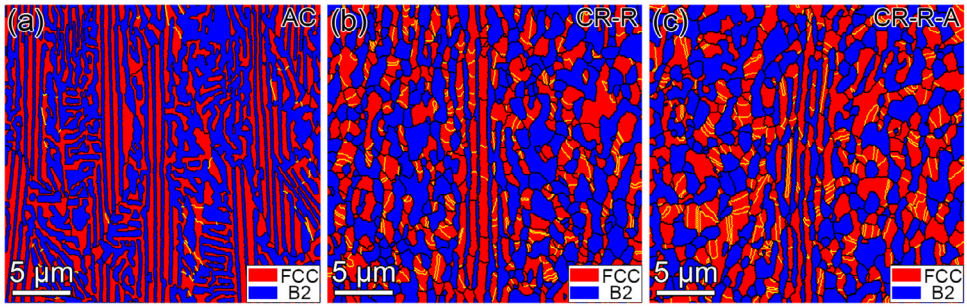

Fig. 1. EBSD maps showing typical microstructures of the $AlCoCrFeNi_{2.1}$ EHEA at different conditions: (a) AC; (b) CR-R; (c) CR-R-A.

ment. A synergetic enhancement of strength and ductility can be achieved in the EHEA $AlCoCrFeNi_{2.1}$.

EHEA with nominal composition $AlCoCrFeNi_{2.1}$ was prepared by repetitive arc melting with high purity constituent elements (better than 99.95%, wt. %) and solidified in a water-cooled copper mold (sample at this condition referred to as AC). The alloy was cold rolled with a thickness reduction of ~70%, and then annealed at 1000 °C for 1 h, followed by water quenching (sample at this condition referred to as CR-R). Aging treatment were conducted at 600 °C for 50 h on the CR-R samples. The samples were vacuum encapsulated in quartz tubes to avoid oxidation and water quenched (sample after aging treatment referred to as CR-R-A). Electron backscatter diffraction (EBSD) characterization was conducted in a Zeiss Supra 35 scanning electron microscope (SEM). The EBSD datum were analyzed with the OIM Analysis software. Transmission electron microscopy (TEM) analysis was performed using the a Tecnai G2 F30 equipped with energy-dispersive spectroscopy (EDS) and an aberration corrected Titan G2 60-300. A Tytron 250 microforce testing system (MTS) was used for uniaxial tensile tests at room temperature with a normal strain rate of 5×10^{-3} s^{-1}. A contactless MTS LX300 laser extensometer was used to calibrate and measure the sample strain upon loading. The gauge section of the dog bone-shaped specimen was 5 mm × 1.5 mm × 0.5 mm.

EBSD phase maps in Fig. 1 show typical microstructures in the AC, CR-R, and CR-R-A samples. As shown in Fig. 1(a), the microstructure of the AC sample exhibits an alternating FCC/B2 lamellar morphology, which is consistent with previous work [18]. The CR-R and CR-R-A samples show similar dual-phase recrystallized heterogeneous structures at the submicron scale as shown in Fig. 1(b) and (c). The heterogeneous structure is characterized with inheriting alternating FCC/B2 lamellae (slightly thickened) embedded with recrystallized grains. In the CR-R sample the average interlamellar grain sizes of the FCC and B2 phases are 0.66 ± 0.15 μm and 0.73 ± 0.12 μm, respectively. Interestingly, the recrystallized dual-phase heterogeneous structure exhibits extraordinary thermal stability. Even after aged at 600 °C for 50 h, the dimensions of the interlamellar grains inside the FCC and B2 phases almost remain unchanged. The interlamellar grain sizes exhibiting 0.66 ± 0.19 μm and 0.81 ± 0.14 μm for the FCC phase and B2 phase, respectively. Also, volume ratio of the FCC phase to the B2 phase in both the CR-R and CR-R-A samples is about 1:1. Detailed microstructures of the AC, CR-R, and CR-R-A samples are shown in Suppl. Fig. S1 (Supplementary Material). The CR-R and CR-R-A samples exhibit similar low dislocation densities with the AC sample, owing to the fully recrystallization after annealing for 1 h at 1000 °C, which is ~ 0.8 T_m (T_m = ~1350 °C [30]).

Fig. 2(a) is a typical scanning transmission election microscopy (STEM) image, showing the heterogeneous structure clearly in the CR-R sample. Selected-area electron diffraction (SAED) patterns in Fig. 2(a) indicate the constituent phases are disordered FCC and B2.

Table 1
Tensile properties of the EHEA $AlCoCrFeNi_{2.1}$.

Conditions	Yield strength (MPa)	Ultimate strength (MPa)	Elongation-to-fracture (%)
AC	646.4	1088.4	17.2
CR-R	732.3	1147.7	24.6
CR-R-A	1008.8	1475.6	19.2

The EDS mapping in Fig. 2(b) demonstrates that the FCC phase are enriched with Co, Cr, and Fe, and the B2 phase are enriched with Al and Ni. No Cr-enriched cluster can be seen in the magnified EDS mapping of the B2 phase in Fig. 2(c).

After 50 h aging treatment at 600 °C, additional superlattice spots, which can be indexed as $L1_2$ ordering, present at the FCC SAED pattern in Fig. 3(a). Fig. 3(b) is a representative dark-field image showing the uniformly-distributed spherical $L1_2$ nanoprecipitate with an average radius of 3.36 ± 1.14 nm in the FCC phase. Fig. 3(c) displays a bright-field image of the B2 phase showing spherical nanoprecipitates with an average radius of 6.56 ± 1.83 nm uniformly distributed there. The inserted high-resolution scanning transmission electron microscopy (HR-STEM) images in Fig. 3(b) and (c) prove that the nanoprecipitates in the B2 phase exhibit a simple BCC structure, and more importantly the $L1_2$ and BCC nanoprecipitates are both highly coherent with their matrix. As shown in Fig. 3(d), the element distributions of the CR-R-A sample are similar with the CR-R sample, demonstrating that the FCC phase still enriches with Co, Cr, Fe, and the B2 phase still enriches with Al and Ni. While, high magnification EDS mapping images of the FCC and B2 phase in Fig. 3(e) and (f) exhibit element segregation between the $L1_2$ precipitates and its FCC matrix, as well as the BCC precipitates and its B2 matrix. Elements Al and Ni tend to segregate into the $L1_2$ precipitates in the FCC phase, and element Cr tends to segregate into the BCC precipitates in the B2 phase. Also, based on statistical analysis on several EDS mapping results, the volume fractions of the $L1_2$ precipitates in the FCC phase and the BCC precipitates in the B2 phase are measured to be ~25.39% and ~17.93%, respectively.

Fig. 4 shows the engineering stress-strain curves of the EHEA $AlCoCrFeNi_{2.1}$ at different conditions, and the results are summarized in Table 1. The yield strength, ultimate strength and elongation-to-fracture of the AC sample are 646.4 MPa, 1088.4 MPa and 17.2%. After recrystallization annealing, the CR-R sample present simultaneous enhancement in strength and ductility, with a yield strength of 732.3 MPa, an ultimate strength of 1147.7 MPa, combined with an elongation-to-fracture of 24.6%. The aging treatments result in striking enhancements in the strength and acceptable sacrifice of ductility. The CR-R-A sample displays the highest yield strength (1008.8 MPa) and the highest ultimate tensile

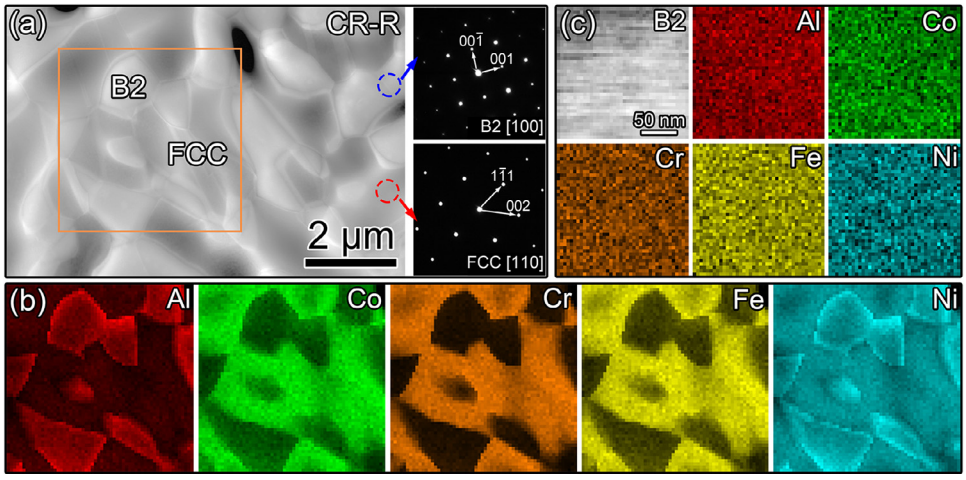

Fig. 2. (a) Typical STEM morphology of the CR-R sample and the corresponding SAED patterns of each constituent phase. (b) EDS mapping of the region marked with an orange square in (a). (c) Magnified STEM image and EDS mapping of the B2 phase.

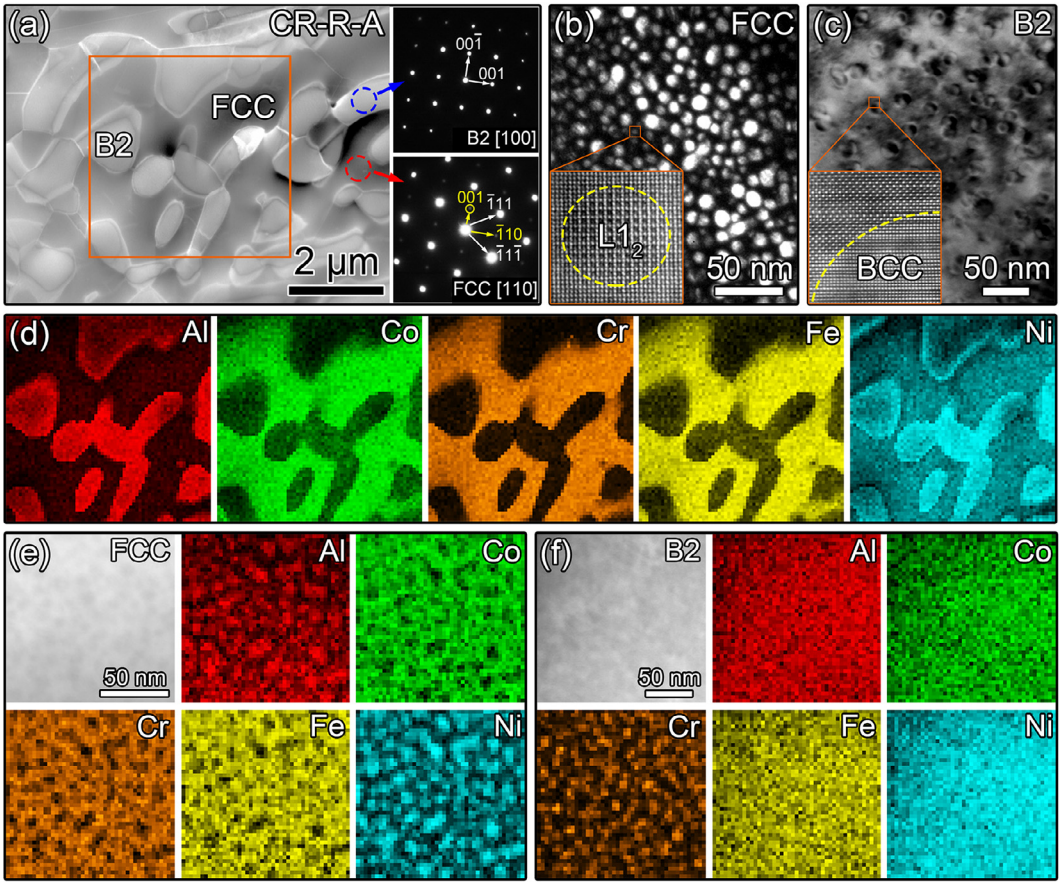

Fig. 3. (a) Typical STEM morphology of the CR-R-A EHEA $AlCoCrFeNi_{2.1}$ and the corresponding SAED patterns of each constituent phase. (b) A dark-field image showing the evenly-distributed nanoprecipitate $L1_2$ phase in the FCC phase, and a HRSTEM image of the nanosized $L1_2$ particle in the FCC phase inserted at the left bottom. (c) A bright-field image of the uniformly-distributed nanoprecipitates in the B2 phase, and a HRSTEM image inserted at the left bottom showing the nanoprecipitate with a BCC structure. (d) EDS mapping of the region marked with an orange square in (a). (e) and (f) are high magnification STEM images and EDS mapping images of the FCC phase and B2 phase, respectively.

strength (1475.6 MPa), and a surprisingly enhanced elongation-to-fracture of 19.2% compared with the AC sample.

The AC sample can achieve a good combination of high strength and good ductility for its typical heterogenous structure characterized with alternating soft FCC and hard B2 lamellae structure. Similar to heterogeneous structure in singe phase alloy, the soft FCC phase will start plastic deformation first, yet be constrained by the surrounding hard B2 phase during tensile deformation [13,31]. Thus, dislocations in the soft FCC phase pile up at the interface, resulting in a long-range back stress [16]. The back stress can strengthen the FCC phase strongly until the surrounding hard B2 phase starts to yield [13,32], resulting in the high yield strength in the AC sample. After both the FCC and B2 phases yielding, the soft FCC phase will carry a larger plastic strain than the hard B2

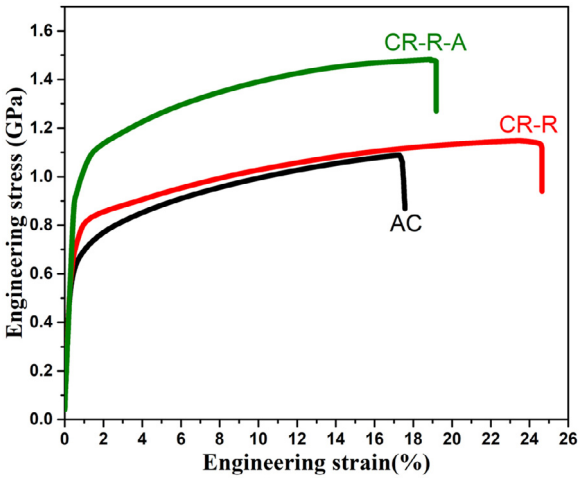

Fig. 4. Engineering stress-strain curves of the EHEA $AlCoCrFeNi_{2.1}$.

phase, creating strain gradient nearby the FCC/B2 phase. The strain gradient nearby the interface will increase continuously with increasing strain partitioning, producing significant back-stress work hardening [13,16,32,33], which help the AC sample to achieve a high ultimate strength and good ductility. As for the CR-R sample, it inherited the alternating FCC/B2 lamellar structure from the AC sample, and achieved full recrystallization inside each lamella during the recrystallization annealing, which generated additional grain boundaries in each lamella. From Fig. 1, we can see obvious eutectic lamella coarsening occurred during the cold rolling and subsequent recrystallization annealing. In metallic materials, the strength significantly depends on the length scale of the characteristic microstructure, such as grain size, lamellar thickness, and so on [34,35]. The grain boundary and phase boundary are strong barriers to the motion of dislocation. The decreasing of the length scale of the characteristic microstructure results in a reduction in dislocation mean-free path, which further leads to the increase in strength [35,36]. Thus, the coarsening of the eutectic lamellae will result in a reduction in strength. On the contrary, the additional generated grain boundaries in each phase inducing a refinement of the interlamellar grain size are supposed to strengthen the material. It seems that the increment of grain boundary density prevails the coarsening of the lamellar structure and causes a slight enhancement of strength in the CR-R sample. In addition, the higher density grain boundaries in the CR-R sample could provide more room to storage dislocations, which help to improve the work hardening capacity of the material. Eventually, the CR-R sample exhibits a reinforced ultimate strength as well as an enhanced ductility compared with the AC sample.

From the above EBSD and TEM results, the microstructure characteristics, such as morphology, phase constituent, phase volume fraction, grain size, and dislocation density of the CR-R and the CR-R-A samples are practically identical at the submicron scale. The only difference presenting at nanoscale is the presence or absence of nanoprecipitates in the FCC and B2 phases. Thus, it can be inferred that the differences of the mechanical properties between the CR-R and the CR-R-A samples mainly originate from the nanoprecipitates. It is clearly demonstrated that the nanoprecipitates in the $L1_2$ and B2 phase result in a strong precipitation strengthening effect and a slight sacrifice of ductility.

The contribution from the precipitate strengthening to the yield strength can be approximately estimated as follows. As shown in Fig. 3, both the FCC and the B2 phase are full of nanoprecipitates and these nanoprecipitates are expected to produce strengthening. The enhancement of strength resulted from the nanoprecipitates can be estimated by the rule of mixture [26]:

$$\sigma_S = f_1 \Delta\sigma_{S1} + f_2 \Delta\sigma_{S2} \tag{1}$$

where σ_S is the overall strength resulting from precipitation strengthening; f_1 and f_2 are the volume fractions of the FCC and B2 phases with the same value 0.5; $\Delta\sigma_{S1}$ is the strength contribution of the $L1_2$ precipitate to the FCC phase; and $\Delta\sigma_{S2}$ is the strength contribution of the BCC precipitate to the B2 phase.

It is well accepted that precipitate can strengthen alloys either through a dislocation Orowan mechanism or particle shearing mechanism [37]. Both the $L1_2$ and BCC precipitates are coherent with their matrices. For coherent precipitate, the operative mechanism can be determined as the one leading to a smaller strength increment [37,38].

When precipitates are bypassed by the dislocations, the yield strength increment caused by Orowan mechanism ($\Delta\sigma_{orw}$) is given as [37]:

$$\Delta\sigma_{orw} = M \frac{0.4Gb}{\pi\sqrt{1-\upsilon}} \frac{ln(2r_m/b)}{\lambda_p} \tag{2}$$

where M is the Taylor factor (3.06 for the FCC matrix [39], 2.8 for the B2 matrix [40]); G is the shear modulus of the matrix (76.9 GPa for the FCC matrix [41], 80 GPa for the B2 matrix [40]); b is the magnitude of Burgers vector (0.254 nm for the FCC matrix, 0.498 nm for the B2 matrix); υ is the Poisson ratio, 0.25; r_m is the mean radius of circular cross-section in a random plane for spherical precipitate, $r_m = (2/3)^{0.5} r$ [42], where r is the mean radius of the precipitates; λ_p is the inter-precipitate spacing, $\lambda_p = 2r_m(\sqrt{\pi/4f} - 1)$ [43], where f is the volume fraction of precipitate in its matrix.

For coherent precipitate sheared by dislocations, the increase in yield strength mainly results from three contributing factors: (1) coherency hardening $\Delta\sigma_{CS}$; (2) modulus hardening $\Delta\sigma_{MS}$; (3) order hardening $\Delta\sigma_{OS}$ [44,45]. The coherency hardening $\Delta\sigma_{CS}$ and modulus hardening $\Delta\sigma_{MS}$ occur before the dislocation shears the precipitate and the order hardening $\Delta\sigma_{OS}$ takes place during shearing. The total strength increment from shearing of the precipitates is the larger one between $\Delta\sigma_{CS} + \Delta\sigma_{MS}$ and $\Delta\sigma_{OS}$ [45–47]. When calculating the contribution of precipitates to yield strength with particle shearing mechanism, as the $L1_2$ precipitate is a superlattice, all the three contributing factors should be considered, while for the disordered BCC precipitate, only the $\Delta\sigma_{CS}$ and $\Delta\sigma_{MS}$ should be considered. The equations for the coherency hardening $\Delta\sigma_{CS}$, modulus hardening $\Delta\sigma_{MS}$ and order hardening $\Delta\sigma_{OS}$ are [44,45]

$$\Delta\sigma_{CS} = M\alpha_\varepsilon (G\varepsilon_c)^{3/2} \left(\frac{rf}{0.5Gb}\right)^{1/2} \tag{3}$$

$$\Delta\sigma_{MS} = 0.0055M(\Delta G)^{\frac{3}{2}} \left(\frac{2f}{G}\right)^{\frac{1}{2}} \left(\frac{r}{b}\right)^{\frac{3m}{2}-1} \tag{4}$$

$$\Delta\sigma_{OS} = 0.81M\frac{\gamma_{APB}}{2b}\left(\frac{3\pi f}{8}\right)^{1/2} \tag{5}$$

where α_ε is a constant, 2.6 [45]; $\varepsilon_c = 2/3\varepsilon$ is the constrained lattice parameter mismatch, with $\varepsilon = \Delta a/a$ (0.084% for the FCC matrix and $L1_2$ precipitate [48], 0.10% for the B2 matrix and BCC precipitate [49]) as the lattice parameter mismatch; $\Delta G = |G - G_p|$ is the shear modulus mismatch between precipitate and its matrix (G_p = 90.2 GPa for the $L1_2$ precipitate [50], G_p = 71 GPa for the BCC precipitate [40]); m is a constant, 0.85 [44]; and γ_{APB}, 175 mJ/m^2 [50], is the antiphase boundary energy of the $L1_2$ precipitate.

The calculated results of the $\Delta\sigma_{orw}$, $\Delta\sigma_{CS}$, $\Delta\sigma_{MS}$ and $\Delta\sigma_{OS}$ are listed in Table 2. From Table 2, we can see that the calculated increments of yield strength for both the $L1_2$ and BCC precipitates from shearing mechanism ($\Delta\sigma_{CS} + \Delta\sigma_{MS}$ or $\Delta\sigma_{OS}$) are

Table 2
Yield strength increments owing to precipitation strengthening.

Phase	$\Delta\sigma_{orw}$	$\Delta\sigma_{CS}$	$\Delta\sigma_{MS}$	$\Delta\sigma_{OS}$	$\Delta\sigma_{CS} + \Delta\sigma_{MS}$	$\Delta\sigma_{S1/2}$
	(MPa)	(MPa)	(MPa)	(MPa)	(MPa)	(MPa)
FCC	6485.6	21.0	134.9	467.0	155.9	467.0
B2	4298.4	21.8	56.6	/	78.4	78.4

much smaller than those from Orowan mechanism ($\Delta\sigma_{orw}$), implying that shearing mechanism is the operative mechanism for both the $L1_2$ and BCC precipitates [37,38]. Thus, the final strength increments are $\Delta\sigma_{S1}$= 467.0 MPa and $\Delta\sigma_{S2}$ = 78.3 MPa for the $L1_2$ precipitate strengthened FCC phase and the BCC precipitate strengthened B2 phase, respectively. The $L1_2$ precipitate have a stronger strengthening effect than the BCC precipitate. Finally, substituting the values of $\Delta\sigma_{S1}$ and $\Delta\sigma_{S2}$ in Eq. (1), the overall strength increment resulting from the $L1_2$ and BCC nanoprecipitates is calculated to be 272.7 MPa, which is agree with the experimental result of 276.5 MPa.

In summary, nanoprecipitates were introduced into each constituent phase of a heterogenous structured dual-phase EHEA $AlCoCrFeNi_{2.1}$ and achieve a simultaneously improvement of strength and ductility in the $AlCoCrFeNi_{2.1}$ EHEA. The achievement can be rationalized as the heterogenous structure strengthens and toughens the material simultaneously, and the precipitates generate additional strong strengthening effect on the material without sacrifice ductility.

Declaration of Competing Interest

The authors declare that they have no known competing financial interests or personal relationships that could have appeared to influence the work reported in this paper.

Acknowledgements

This work was supported financially by the National Natural Science Foundation of China (No. 51771201), Joint Research Fund Liaoning-Shenyang National Laboratory for Materials Science (No. 20180510059). We thank to Mr. Bo Wu and Mr. Lixin Yang for transmission electron microscope technical support.

Supplementary materials

Supplementary material associated with this article can be found, in the online version, at doi:10.1016/j.scriptamat.2020.04.035.

References

[1] J.W. Yeh, S.K. Chen, S.J. Lin, J.Y. Gan, T.S. Chin, T.T. Shun, C.H. Tsau, S.Y. Chang, Adv. Eng. Mater 6 (5) (2004) 299–303.
[2] B. Gludovatz, A. Hohenwarter, D. Catoor, E.H. Chang, E.P. George, R.O. Ritchie, Science 345 (6201) (2014) 1153–1158.
[3] L.X. Yang, H.L. Ge, J. Zhang, T. Xiong, Q.Q. Jin, Y.T. Zhou, X.H. Shao, B. Zhang, Z.W. Zhu, S.J. Zheng, X.L. Ma, J. Mater. Sci. Technol 35 (3) (2019) 300–305.
[4] Y. Zhang, Y.J. Zhou, J.P. Lin, G.L. Chen, P.K. Liaw, Adv. Eng. Mater 10 (6) (2008) 534–538.
[5] M.C. Gao, D.E. Alman, Entropy 15 (10) (2013) 4504–4519.
[6] Y.P. Wang, B.S. Li, H.Z. Fu, Adv. Eng. Mater 11 (8) (2009) 641–644.
[7] O.N. Senkov, G.B. Wilks, J.M. Scott, D.B. Miracle, Intermetallics 19 (5) (2011) 698–706.
[8] Y.D. Wu, Y.H. Cai, T. Wang, J.J. Si, J. Zhu, Y.D. Wang, X.D. Hui, Mater. Lett 130 (2014) 277–280.
[9] S.J. Sun, Y.Z. Tian, H.R. Lin, S. Lu, H.J. Yang, Z.F. Zhang, Scr. Mater 163 (2019) 111–115.
[10] K. Lu, Science 345 (6203) (2014) 1455–1456.
[11] R. Cao, Q. Yu, J. Pan, Y. Lin, A. Sweet, Y. Li, R.O. Ritchie, Mater. Today 32 (2020) 94–107.
[12] S.J. Zheng, I.J. Beyerlein, J.S. Carpenter, K.W. Kang, J. Wang, W.Z. Han, N.A. Mara, Nat. Commun (2013) 4.
[13] X. Wu, M. Yang, F. Yuan, G. Wu, Y. Wei, X. Huang, Y. Zhu, Proc. Natl. Acad. Sci. USA 112 (47) (2015) 14501–14505.
[14] K. Park, M. Nishiyama, N. Nakada, T. Tsuchiyama, S. Takaki, Mater. Sci. Eng. A 604 (2014) 135–141.
[15] Y.M. Wang, M.W. Chen, F.H. Zhou, E. Ma, Nature 419 (6910) (2002) 912–915.
[16] X.L. Wu, Y.T. Zhu, Mater. Res. Lett 5 (8) (2017) 527–532.
[17] I. Basu, V. Ocelík, J.T. De Hosson, Acta Mater 157 (2018) 83–95.
[18] Y.P. Lu, X.Z. Gao, L. Jiang, Z.N. Chen, T.M. Wang, J.C. Jie, H.J. Kang, Y.B. Zhang, S. Guo, H.H. Ruan, Y.H. Zhao, Z.Q. Cao, T.J. Li, Acta Mater 124 (2017) 143–150.
[19] X. Jin, Y. Zhou, L. Zhang, X. Du, B. Li, Mater. Lett 216 (2018) 144–146.
[20] E. Ma, X. Wu, Nat. Commun 10 (1) (2019) 5623.
[21] T. Bhattacharjee, I.S. Wani, S. Sheikh, I.T. Clark, T. Okawa, S. Guo, P.P. Bhattacharjee, N. Tsuji, Sci. Rep. 8 (1) (2018) 3276.
[22] P. Shi, W. Ren, T. Zheng, Z. Ren, X. Hou, J. Peng, P. Hu, Y. Gao, Y. Zhong, P.K. Liaw, Nat. Commun. 10 (1) (2019) 489.
[23] S.R. Reddy, S. Yoshida, T. Bhattacharjee, N. Sake, A. Lozinko, S. Guo, P.P. Bhattacharjee, N. Tsuji, Sci. Rep. 9 (1) (2019) 11505.
[24] T. Xiong, S.J. Zheng, Y.T. Zhou, J.C. Pang, Q.Q. Jin, H.L. Ge, X.D. Zheng, L.X. Yang, I.J. Beyerlein, X.L. Ma, Mater. Sci. Eng. A 720 (2018) 231–237.
[25] S.H. Jiang, H. Wang, Y. Wu, X.J. Liu, H.H. Chen, M.J. Yao, B. Gault, D. Ponge, D. Raabe, A. Hirata, M.W. Chen, Y.D. Wang, Z.P. Lu, Nature 544 (2017) 460–464.
[26] J.Y. He, H. Wang, H.L. Huang, X.D. Xu, M.W. Chen, Y. Wu, X.J. Liu, T.G. Nieh, K. An, Z.P. Lu, Acta Mater 102 (2016) 187–196.
[27] X. Gao, Y. Lu, B. Zhang, N. Liang, G. Wu, G. Sha, J. Liu, Y. Zhao, Acta Mater 141 (2017) 59–66.
[28] B. Gwalani, V. Soni, D. Choudhuri, M. Lee, J.Y. Hwang, S.J. Nam, H. Ryu, S.H. Hong, R. Banerjee, Scr. Mater. 123 (2016) 130–134.
[29] I.S. Wani, T. Bhattacharjee, S. Sheikh, P.P. Bhattacharjee, S. Guo, N. Tsuji, Mat. Sci. Eng. a-Struct. 675 (2016) 99–109.
[30] Y.P. Lu, Y. Dong, S. Guo, L. Jiang, H.J. Kang, T.M. Wang, B. Wen, Z.J. Wang, J.C. Jie, Z.Q. Cao, H.H. Ruan, T.J. Li, Sci. Rep. 4 (2014) 6200.
[31] M.X. Yang, D.S. Yan, F.P. Yuan, P. Jiang, E. Ma, X.L. Wu, Proc Natl Acad Sci USA 115 (28) (2018) 7224–7229.
[32] E. Ma, T. Zhu, Mater. Today 20 (6) (2017) 323–331.
[33] Y. Zhu, X. Wu, Mater. Res. Lett. 7 (10) (2019) 393–398.
[34] I. Basu, V. Ocelík, J.T.M. De Hosson, Acta Mater 150 (2018) 104–116.
[35] W. Yang, I.J. Beyerlein, Q. Jin, H. Ge, T. Xiong, L. Yang, J. Pang, Y. Zhou, X. Shao, B. Zhang, S. Zheng, X. Ma, Scr. Mater. 166 (2019) 73–77.
[36] S.J. Zheng, R.F. Zhang, R. Huang, T. Taniguchi, X.L. Ma, Y. Ikuhara, I.J. Beyerlein, Appl. Phys. Lett. 109 (8) (2016).
[37] K. Ma, H. Wen, T. Hu, T.D. Topping, D. Isheim, D.N. Seidman, E.J. Lavernia, J.M. Schoenung, Acta Mater 62 (2014) 141–155.
[38] T.H. Courtney, Mechanical behavior of materials, Long Grove, Waveland, 2005.
[39] R.E. Stoller, S.J. Zinkle, J. Nucl. Mater. 283 (2000) 349–352.
[40] S.-I. Baik, S.-Y. Wang, P.K. Liaw, D.C. Dunand, Acta Mater 157 (2018) 142–154.
[41] H.Y. Yasuda, K. Shigeno, T. Nagase, Scr. Mater. 108 (2015) 80–83.
[42] P.B. Hirsch, F.J. Humphreys, The Physics and Strength of Plasticity, MIT Press, Cambridge, 1969.
[43] R.H.L. Brown, Strengthening Methods in Crystals, Elsevier, Amsterdam, 1971.
[44] A.J. Ardell, Metallurg. Trans. A 16 (12) (1985) 2131–2165.
[45] H.M. Wen, T.D. Topping, D. Isheim, D.N. Seidman, E.J. Lavernia, Acta Mater 61 (8) (2013) 2769–2782.
[46] D.N. Seidman, E.A. Marquis, D.C. Dunand, Acta Mater 50 (16) (2002) 4021–4035.
[47] C.B. Fuller, D.N. Seidman, D.C. Dunand, Acta Mater 51 (16) (2003) 4803–4814.
[48] I.V. Kireeva, Y.I. Chumlyakov, Z.V. Pobedennaya, A.V. Vyrodova, Mater. Sci. Eng. A 772 (2020) 138772.
[49] R. Fischer, G. Frommeyer, A. Schneider, Mater. Sci. Eng. A 327 (1) (2002) 47–53.
[50] J.-S. Wang, Acta Mater 46 (8) (1998) 2663–2674.